Age offsets among different biogenic and lithogenic components of sediment cores revealed by numerical modeling

C. Heinze,[1] I. Kriest,[2] and E. Maier-Reimer[3]

Received 17 July 2008; revised 14 August 2009; accepted 2 September 2009; published 17 December 2009.

[1] For modeled sediment cores of the open ocean, a method for predicting simultaneously the ages of four different solid sediment compounds with respect to their depositional year onto the sediment surface is presented. The simulation of time-dependent age distribution in the sediment mixed layer and the eventually accumulating sediment is a prerequisite of a proper data assimilation of marine sediment core data into predictive climate models. Through such a data assimilation, marine paleoclimate data could then be efficiently used in order to optimally determine adjustable model parameters. The age simulation is based on a passive tracer transport method taking into account varying vertical advection rates within the sediment top layers, chemical pore water reactions, and bioturbation. It turns out that different weight fractions of the modeled sediment have different ages in one horizontal geometric depth-in-core level depending on the particle rain onto the sediment and the reactivity of the material within the sediment pore waters. For simultaneous consideration of paleoclimatic tracers associated within one and the same weight fraction, e.g., for calcium carbonate, tracers such as foraminiferal $\delta^{13}C$, and calcium carbonate weight percentages, this may not be critical. However, for simultaneous consideration of calcium carbonate and opal weight percentages, the age difference in the observed weight fractions may have to be corrected. The age offset between $CaCO_3$ and opal depends critically on the sediment accumulation rate. Low-accumulation sites are more strongly affected than high-accumulation sites.

Citation: Heinze, C., I. Kriest, and E. Maier-Reimer (2009), Age offsets among different biogenic and lithogenic components of sediment cores revealed by numerical modeling, *Paleoceanography*, *24*, PA4214, doi:10.1029/2008PA001662.

1. Introduction

[2] A most accurate projection of future climate changes for given emission rates of greenhouse gases is a key challenge for the present scientific climate and Earth system modeling community. Though not all processes (these include also feedback processes) which will be of primary importance in a future climate have suitable paleoanalogues [*Crowley*, 1990], a systematic calibration of prognostic climate models through the observed paleorecord is intriguing. If we could seamlessly simulate past climates, the present climate, and the future evolution with one calibrated model system, the respective future scenarios would be more credible than scenarios provided by model systems which have not shown their ability to reproduce past climatic changes properly.

[3] In particular, it is important to calibrate the models' sensitivities with respect to changes in external forcing and internal perturbations. With sensitivities we mean here the first and second derivatives of key state variables of the climate system, such as surface air and water temperatures, carbon fluxes between the different Earth system reservoirs, wind velocities and directions etc. Through the systematic data assimilation of the paleoclimatic record from marine sediment core data, but also from ice core data and terrestrial paleoclimate data, the sensitivity behavior of Earth system models could potentially be significantly improved by appropriate correction of model parameters governing the process representations. At least, we can aim at ultimately incorporating all the knowledge of past climates into prognostic Earth system modeling frameworks.

[4] Though a number of paleoclimatic research projects were carried out under the motivation of understanding the past as a necessary prerequisite for correctly predicting the future, attempts of direct data assimilation of paleoclimatic data into models, have been limited [*LeGrand and Wunsch*, 1995; *Winguth et al.*, 1999; *Grieger and Niebler*, 2003]. This limitation is due to several difficulties, such as the extreme logistical and computational resources for a time-dependent assimilation with coupled general circulation models or constructing respective adjoint models, and the lack of fast but detailed enough Earth system models to allow a quantitatively correct regional climate simulation while retaining global coverage. The combination of new generations of supercomputers and the experience from coarse resolution fast global 3-D Earth system models [e.g., *Mikolajewicz et al.*, 2007] bring the direct paleoclimate data assimilation closer to the realm of concrete

[1]Geophysical Institute and Bjerknes Centre for Climate Research, University of Bergen, Bergen, Norway.
[2]Leibniz Institute of Marine Sciences at University of Kiel (IFM-GEOMAR), Kiel, Germany.
[3]Max Planck Institute for Meteorology, Hamburg, Germany.

0883-8305/09/2008PA001662

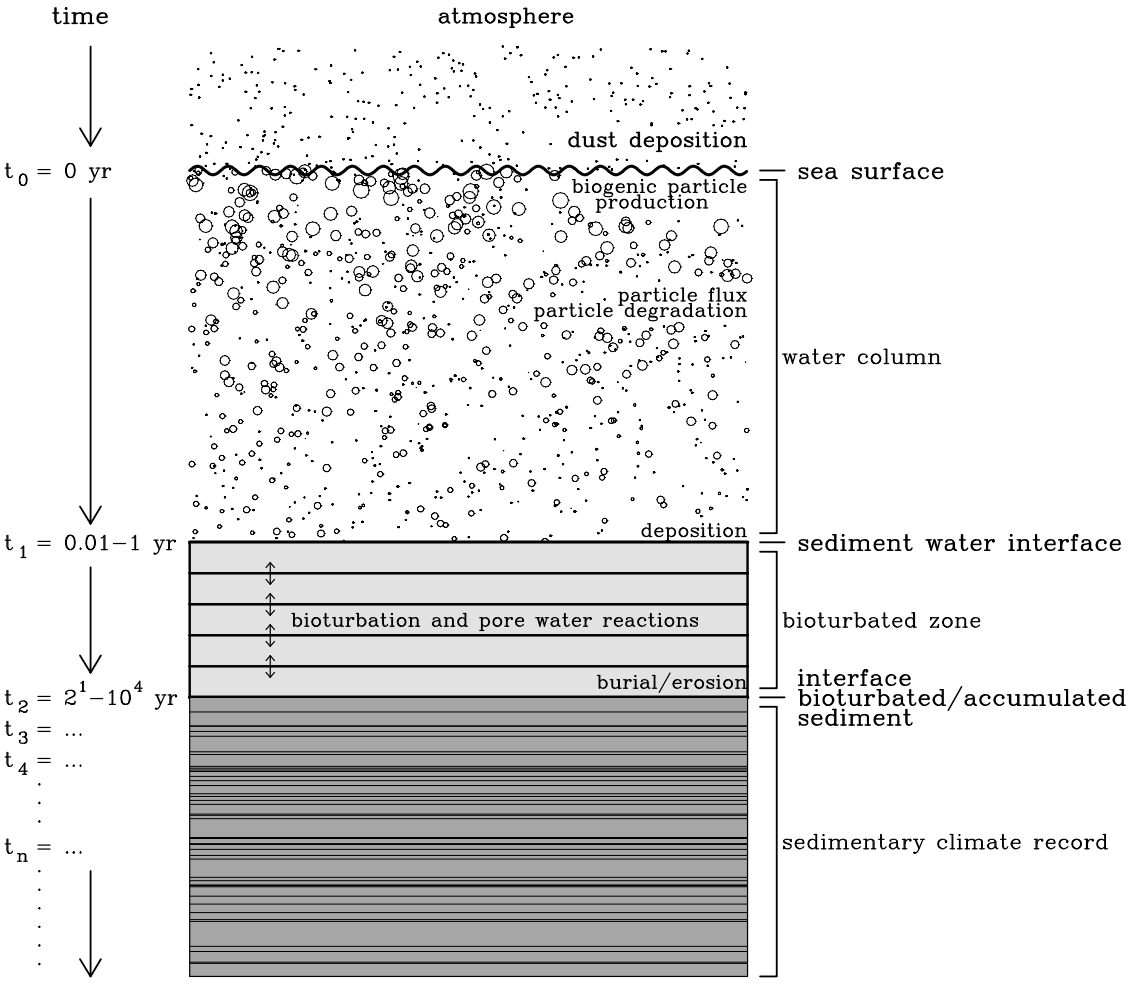

Figure 1. Schematic of the various ocean compartments of importance for building up the paleosediment record. In order to date correctly the sediment compounds in the solidified sediment below the sediment mixed layer, one needs to hand down the correct vintage year of the respective particles which enter the top sediment from the water column. Please see the increasing time indicator vertically increasing from top to bottom on the left side of the diagram.

feasibility. In order to directly assimilate the marine paleoclimatic record, the method of synthetic sediment cores on a global basis was developed [*Heinze*, 2001]. This method enables to "drill" into modeled marine sediment strata and "recover" artificial sediment cores, which then can directly be compared with data from the real world. With the term data assimilation we focus in our context here on the optimal estimation of adjustable model parameters, such as biogeochemical rate constants or even the atmospheric forcing fields, and not the interpolation of the sediment core record as such.

[5] A difficulty in the practical use of the method was on how to associate modeled ages of sediment compounds within the simulated sediment mixed layer (bioturbated zone) and at the transfer from the model sediment mixed layer to the solidified sediment with the real ages of the measured sediment compositions [see *Heinze*, 2001]. If one, e.g., would simply relate the age of accumulating material (i.e., of material leaving the sediment mixed layer and arriving in the "quasi-unreactive" solid material further downcore) in the model with the actual date (time step) of the respective model run, then one would assume a quasi-instantaneous transfer of material from the sediment water interface to the interface between sediment mixed layer and the "solidified/unreactive sediment column." In reality, however, this transfer can take up to several thousand years depending on the rain rate of particles from the water column on to the sediment surface and the subsequent pore water reactions as well as transport processes within the top sediment (Figure 1). The accumulating sediment weight fractions, therefore, would be too young and could not be properly related with the actual processes going on in the model ocean atmosphere system. Moreover, particles from different "vintage years" would be mixed through bioturbation so that the finally accumulating sediment material would only have an approximate vintage year averaged over many years. For model studies involving single reactive species, such a more realistic down core age tracer transport

has been implemented in biogeochemical ocean components of coarse resolution Earth system models (for $CaCO_3$ [*Ridgwell*, 2007a] and for opal [*Ridgwell*, 2007b]).

[6] Also in general, the age structure of the sediment record is of key importance for a correct interpretation of the marine sediment core record with respect to past climatic and environmental change. Recently, a number of experimental studies suggested considerable age offsets between different sediment weight fractions at identical geometric downcore depth [*Ingalls et al.*, 2004; *Mollenhauer et al.*, 2007]. Therefore, it is intriguing to understand the reason for such offsets in order to synchronize all measured variables from sediment core analysis correctly.

[7] We try here to provide a method for handling and determining the age of modeled sediment consisting of four different weight fractions ($CaCO_3$, opal, organic carbon, and clay), so that the difficulties for associating a certain sediment compound in the model with a specific real year of past Earth's history can be overcome. We will first describe briefly the global sediment model as a component for an Earth system modeling framework and afterward present the age modeling through a passive tracer simulation technique. In the second part we will show some model results for a steady state perpetual preindustrial run. In the third part, sensitivity experiments will be carried out to show the role of certain model parameters for the age distribution in the bioturbated sediment zone.

2. Model Description and Method

[8] We employ here the "HAMOCC" global biogeochemical ocean model [*Maier-Reimer*, 1993; *Maier-Reimer et al.*, 2005]. In order to keep the computational effort for equilibrating the sediment coverage in practical limits, we use the model in its annually averaged version "HAMOCC2s" [*Heinze et al.*, 1999, 2003]. The respective velocity and thermohaline fields are read from an input data set which represents the preindustrial circulation. These fields are the annually averaged result from forcing the large-scale geostrophic dynamical ocean general circulation model with climatological atmospheric data (details are given by *Winguth et al.* [1999] for their "interglacial first guess" circulation). The effect of deep convective mixing at high latitudes is accounted for also in the annually averaged velocity field, which is used for transporting the dissolved tracer substances within the model water column. The horizontal resolution is $3.5° \times 3.5°$. The water column is structured into 11 layers (centered at 25, 75, 150, 250, 450, 700, 1000, 2000, 3000, 4000, and 5000 m). The bioturbated top sediment zone is divided into 10 layers which are separated by interfaces at 0, 0.3, 0.6, 1.1, 1.6, 2.1, 3.1, 4.1, 5.1, 7.55, and 10 cm "downcore." We thus make the simplifying assumption that no pore water reactions take place below 10 cm depth in the sediment [see, e.g., *Smith and Rabouille*, 2002; *Boudreau*, 1997]. The biogeochemical model includes the processes air-sea gas exchange, biogenic particle export production out of the ocean surface layer, particle flux through the water column and particle degradation by dissolution as well as remineralization, transport of dissolved substances with the ocean currents, deposition of particulate constituents on the ocean floor, pore water chemistry and diffusion, advection of solid sediment weight fractions, bioturbation, and sediment accumulation (export out of the sediment mixed layer).

[9] The model as used in the present application predicts the following tracer concentrations in the atmosphere, the ocean water column, the sediment pore waters and the solid sediment: atmosphere, $^{12}CO_2$ (carbon dioxide), $\delta^{13}CO_2$, and O_2; water column, DIC (dissolved inorganic carbon), POC (particulate organic carbon), DOC (dissolved organic carbon), $CaCO_3$ (calcium carbonate or particulate inorganic carbon) of ^{12}C and ^{13}C, dissolved oxygen O_2, dissolved PO_4^{3-} as biolimiting nutrient, silicic acid $Si(OH)_4$ and opal (biogenic particulate silica BSi); sediment pore waters, the same dissolved substances as in the water column; and solid sediment, clay, $CaCO_3$, opal, and organic carbon. For inorganic carbon chemistry, the reaction constants for the dissociation of carbonic and boric acid according to *Mehrbach et al.* [1973], the solubility product for $CaCO_3$ after *Ingle* [1975], and the pressure dependencies of *Edmond and Gieskes* [1970] were applied. In the advection scheme and for the other chemical reactions, DIC and TAlk were used as "master tracers" form which derived quantities such as the CO_3^{2-} concentration and the pH value where computed through a Newton-Raphson algorithm whenever needed. The ocean surface and water column processes and the pore water chemistry are represented through parameterizations as described in previous applications of the model [*Heinze et al.*, 1999, 2003, 2006]. The process parameterizations are described below in more detail. Numerical values for tunable model parameters are summarized in Table 1.

2.1. Air-Sea Gas Exchange

[10] Between the two reservoirs atmosphere and ocean surface layer CO_2 and oxygen can be exchanged. For CO_2 the following formulation is used:

$$F_{CO2} = k_{CO2} \cdot \left(pCO_{2,air} - pCO_{2,water}\right) \quad (1)$$

where F_{CO2} is the carbon dioxide flux across air/sea interface and k_{CO2} is the specific gas exchange rate. The CO_2 partial pressure is calculated from the free carbon dioxide concentration in seawater following Henry's law by use of the solubility α [*Weiss*, 1974]:

$$pCO_{2,water} = \alpha \cdot [CO_2] \quad (2)$$

For oxygen, the gas exchange between ocean and atmosphere is modeled by the following expression:

$$\begin{aligned} F_{O2} &= k_{O2} \cdot \left(C_{O2,equilibrium} - C_{O2,actual}\right) \\ C_{O2,equilibrium} &= f(T,S) \cdot C_{O2,atmosphere}(t) \end{aligned} \quad (3)$$

where F_{O2} is the net gas flux between sea surface and atmosphere, k_{O2} is the mean gas transfer velocity, $C_{O2,equilibrium}$ and $C_{O2,actual}$ are the oceanic oxygen concentrations for solubility equilibrium with the atmosphere and the actual observed (or modeled) value,

Table 1. Model Parameter Values as Set for the Control or Standard Run

Tunable Model Parameter	Parameter Symbol	Control Run Value
Specific gas exchange rate for CO_2	k_{CO2}	0.0704 (mol m^{-2} a^{-1} ppm^{-1})
O_2 gas transfer velocity	k_{O2}	250 m yr^{-1}
Threshold value S_{opal} of particle export production ratio for the onset of $CaCO_3$ production (see equation (7))	C(opal):C(POC)	0.6
Maximum possible production rain ratio (see equation (8))	C($CaCO_3$):C(POC) R	0.26
Global weathering input of Si	-	4.5×10^{12} mol Si yr^{-1}
Global weathering input of $CaCO_3$	-	15×10^{12} mol C yr^{-1}
Global weathering input of POC	-	5×10^{12} mol C yr^{-1}
$Si(OH)_4$ saturation concentration	C_{sat}	800 μmol yr^{-1}
Degradation rate of $CaCO_3$ in water column	r_{CaCO3}	310.3 yr^{-1}
Minimum value for $CaCO_3$ undersaturation in water column	Ω_{min}	0.062
Degradation rate of opal in water column	r_{opal}	23 yr^{-1}
Degradation rate of POC water column	r_{POC}	70 yr^{-1}
Sinking velocity of particulate matter in water column	w_M	120 m d^{-1}
Dissolution rate constant for $CaCO_3$ sediment	r_c*	368
Dissolution rate constant for opal sediment	r_c*	13 yr^{-1}
Dissolution rate constant for organic carbon sediment	r_c*	70 yr^{-1}
Degradation rate constant for dissolved organic carbon in the water column	-	0.05 yr^{-1}
Diffusion constant for pore waters	D_w	8×10^{-6} cm^2 s^{-1}
Coefficient for explicit bioturbation	D_b	40 cm^2 1000 yr^{-1}

respectively, $f(T,S)$ is the measured solubility which is a function of the seawater temperature and salinity, and $C_{O2,atmosphere}(t)$ is the O_2 concentration in the troposphere. $f(T,S)$ is prescribed according to *Weiss* [1970]. In the model, the O_2 gas exchange is implemented according to the analytical solution of the differential equation

$$\frac{dC}{dt} = F/\Delta z,$$

where C is the gas concentration in mol cm^{-3}, F the flux in mol cm^{-2} s^{-1} of gas into (out of) a control volume of 1 cm length, 1 cm width and thickness Δz in cm. The corresponding numerical scheme then is

$$C^{new} = C_{equilibrium} + \left(C^{old} - C_{equilibrium}\right) \cdot e^{(-k_{av}/\Delta z)\cdot \Delta t} \quad (4)$$

where Δt is the time step (here 1 year) and Δz is the thickness of the layer affected by gas exchange. Δz was set to 50 m in cases of hydrostatic stability and to the maximum depth of the convective layer if convective adjustment was applied at the respective grid point. The model atmosphere is represented through a 1 layer box over each grid point. After each time step, zonal averages are computed and meridional gas transport is simulated through meridional diffusion.

2.2. Biogenic Particle Export Production and Particle Flux (Including Particle Degradation and Deposition to Sediment)

[11] In the annually averaged model only export production of biogenic particles is modeled. Particle production takes place in the model surface layer representing the euphotic zone. Phosphate serves as biolimiting nutrient. POC (particulate organic carbon) and opal export productions are simulated on the basis of Michaelis Menten kinetics for nutrient uptake [e.g., *Parsons and Takahashi*, 1973]:

$$P_{POC} = \frac{V_{\max}^{POC} \cdot \left[PO_4^{3-}\right]^2 \cdot Red(C:P)}{K_s^{POC} + \left[PO_4^{3-}\right]} \quad (5)$$

$$P_{opal} = \frac{V_{\max}^{opal} \cdot \left[Si(OH)_4\right]^2}{K_s^{opal} + \left[Si(OH)_4\right]} \quad (6)$$

where P_{POC} and P_{opal} are the POC and opal export production rates (mol l^{-1} yr^{-1}), $Red(C:P)$ is the Redfield ratio C:P, $V_{\max}^{POC}$ and $V_{\max}^{opal}$ are the maximum uptake rate of phosphate and silicic acid from the water column (yr^{-1}), and K_s^{POC} as well as K_s^{opal} are the respective half saturation constants. The parameters $V_{\max}^{POC}$, $V_{\max}^{opal}$, K_s^{POC}, and K_s^{opal} are scaled with sea surface temperature as described by *Heinze et al.* [2003].

[12] The export production of $CaCO_3$ is coupled to the local production ratio P_{opal}/P_{POC}. It starts to increase gradually (parameter R see below) if P_{opal}/P_{POC} sinks below a threshold value S_{opal}, i.e., when not enough silicic acid is available in the ocean surface layer to fuel full diatom growth:

$$P_{CaCO_3} = P_{POC} \cdot R \cdot \left(1 - \frac{P_{opal}/P_{POC}}{S_{opal}}\right), \quad \text{for} \quad P_{opal}/P_{POC} < S_{opal}; \quad (7)$$

$$P_{CaCO_3} = 0, \quad \text{for} \quad P_{opal}/P_{POC} \geq S_{opal} \quad (8)$$

where R is the maximum possible rain ratio C($CaCO_3$): C(POC) and S_{opal} is the threshold value of P_{opal}/P_{POC} for gradual onset of $CaCO_3$ production.

[13] Particle fluxes are simulated through balance equations for sinking particulate matter M_{settle}, where M_{settle} stands for one of the different particle species POC_{settle}, $CaCO_{3settle}$, $opal_{settle}$, and $clay_{settle}$. The generic balance equation for M_{settle} is

$$\begin{aligned} \frac{d\,M_{settle}}{dt} &= gain - loss \\ \frac{d\,M_{settle}}{dt} &= P_M - \frac{w_M}{\Delta z_0}\cdot M_{settle} - r_M \cdot M_{settle} \\ &\quad (for\ surface\ layer) \\ \frac{d\,M_{settle}}{dt} &= w_M \cdot \frac{\partial M_{settle}}{\partial z} - r_M \cdot M_{settle} \\ &\quad (for\ other\ layers) \end{aligned} \tag{9}$$

where w_M is the particle settling velocity (m yr^{-1}), r_M is the reaction rate constant (yr^{-1}) for degradation of particulate matter, and P_M is the export production rate in the uppermost layer, where again M can stand for one of the particle species POC, $CaCO_3$, opal, and clay. P_{clay} is the dust input from the atmosphere which is prescribed here as the interglacial or modern dust deposition field from *Mahowald et al.* [1999]. Clay material is assumed to be chemically inert in this study. Δz_0 is the thickness of the euphotic zone (m). This system of equations (9) is readily solvable with an implicit numerical scheme. For the parameterization of $CaCO_3$ dissolution in the water column we use a saturation-dependent redissolution rate constant:

$$r_{CaCO3} = k_{CaCO3} \cdot (1 - \Omega) \tag{10}$$

where k_{CaCO3} is a fixed standard rate constant, and $(1 - \Omega) = ([CO_3^{2-}]_{sat} - [CO_3^{2-}])/[CO_3^{2-}]_{sat}$ is the degree of undersaturation We apply a formal minimum value of 0.062 for the undersaturation thus allowing for some $CaCO_3$ dissolution in oversaturated waters. The amount of particles raining out of the lowest wet layer in the water column provide the source term Q for particles added to the top sediment layer (see below). The reaction losses in (9) for settling particulate material are balanced by appropriate source terms for dissolved species within the water column (i.e., for TAlk, DIC, phosphate, oxygen, and silicic acid).

2.3. Sediment Pore Water Chemistry and Diffusion

[14] The sediment processes are simulated with the method as described by *Heinze et al.* [2003], closely following conceptually *Archer et al.* [1993], however, with more efficient numerics following *Maier-Reimer et al.* [2005]. A slight modification was added in case of chemical erosion of sediment (see further below). For the simulated sediment, we assume a prescribed, fixed (in time) porosity profile [after *Ullmann and Aller*, 1982]. The sediment model is based on the equilibrium [see *Archer et al.*, 1993]:

$$sediment\ accumulation = deposition - redissolution$$

The basic equations for a solid sediment component expressed in moles per unit volume of sediment S_* and the related concentration of the corresponding dissolved substance C within the pore water are

$$\frac{dS_*}{dt} = D_B \frac{\partial^2 S_*}{\partial z^2} - \frac{\partial}{\partial z}\left(w \cdot S_*\right) - G \tag{11}$$

$$\frac{dC}{dt} = \frac{\partial}{\partial z}\left(D_W \frac{\partial C}{\partial z}\right) + G \tag{12}$$

where D_B is the diffusion coefficient for bioturbation, w the vertical advection velocity of solid compound, and G the reaction rate (with S_*, C, and G reported here in relation to full sediment volume of a given sediment layer for sake of simplicity; within the model, the differential volumes for dissolved and solid substances according to the porosity profile are taken into account, of course). Equations (11) and (12) are solved numerically using operator splitting, i.e., pore water reactions plus pore water diffusion, bioturbation, and sediment advection plus accumulation are carried out subsequently in different steps. Chemical pore water reactions and pore water diffusion are carried out simultaneously in an implicit numerical algorithm enabling time efficient integration of the model. The prognostic equations for solid sediment concentrations S_* (organic carbon, $CaCO_3$, opal, and clay) and for dissolved components C (TAlk, DIC, phosphate, oxygen, and silicic acid) are coupled with each other by the reaction rates. Rather than computing directly the diffusion of the dissolved substance, we here determine the diffusive transport of the respective deviations from saturation simultaneously with the reduction of this deviation due to chemical pore water reactions:

$$\frac{dU}{dt} = \frac{\partial}{\partial z}\left(D_W \frac{\partial U}{\partial z}\right) - G \tag{13}$$

where U is the deviation of the saturation concentration C_{sat} from the actual concentration C (mol l^{-1}), G is the reaction rate (sink for U from dissolution of solid material) (mol l^{-1} yr^{-1}) and D_W is the diffusion coefficient for pore water transport. As the reaction rate is proportional to the degree of undersaturation this formulation facilitates use of an implicit numerical scheme regardless of the size of the time step and reaction kinetics without the risk of achieving negative tracer concentrations. The pore water diffusion coefficient D_W is set to 8×10^{-6} cm^2 s^{-1} for all pore water tracers which is in the range of the values given for individual tracer species by *Li and Gregory* [1974]. The change of a solid sediment component due to pore water reactions and particle deposition corresponding to equation (13) is

(bioturbation is carried out in a separate step and is hence not stated in the following formula)

$$\frac{dS_*}{dt} = -G + Q \tag{14}$$

where S_* is the solid sediment component expressed in the same units as U (mol l^{-1}), G is the reaction rate (sink due to dissolution) (mol l^{-1} yr^{-1}), and Q is the gain from particle rain (mol l^{-1} yr^{-1}) (the latter is active only for the uppermost sediment layer). The amount of matter subject to dissolution G per unit time depends on parameter r_c*, the deviation from saturation concentration U, and the amount of solid material available S_*:

$$G = r_c^* \cdot U \cdot S_* \tag{15}$$

where for r_c* we have

$$r_c^* = \frac{r_c}{C_{sat}} \tag{16}$$

with r_c the reaction rate constant (yr^{-1}) and C_{sat} the saturation concentration in solution (mol l^{-1}). For opal dissolution a solubility C_{sat} of 800 μmol is used [cf. *Dixit et al.*, 2001]. The "saturation concentration" for organic carbon is given by the availability of oxygen (we neglect here anaerobic respiration and associated effects of denitrification and sulfate reduction). For $CaCO_3$, the saturation concentration of carbonate is computed from the in situ solubility product after *Ingle* [1975] with pressure correction after *Edmond and Gieskes* [1970] (see equation (10)). The coupled equations (13) and (14) are discretized and solved numerically. The pore water diffusion is not carried out as a boundary condition problem. The uppermost "pore water box" was represented by the respective lowermost wet grid box in the water column directly overlying the top sediment layer, so that free water column and sediment pore waters can directly communicate with each other and full mass conservation is achieved.

2.4. Bioturbation

[15] Bioturbation is parameterized through vertical Fickian "diffusion" of solid material as in the work by *Heinze et al.* [1999, 2003], where the solid material in neighboring layers is slowly mixed in proportion to the prevailing weight fractions in these layers so that within the bioturbated zone, mass conservation is guaranteed:

$$\frac{dS_*}{dt} = \frac{\partial}{\partial z}\left(D_B \frac{\partial S_*}{\partial z}\right) \tag{17}$$

with D_B being the bioturbation coefficient. Bioturbation is carried out after the vertical advection step described further below. We apply here no parameterization of nonlocal mixing [e.g., *Boudreau and Imboden*, 1987] as reliable statistics on pelagic sediments for this process are not available. Grain size-dependent bioturbation can cause phase shifts and relative signal attenuation between different size fractions included in sediment records [e.g., *Bard*, 2001]. The associated effect is most important when abrupt events are mapped onto the sedimentary record. We do not include grain size-dependent particle fluxes or grain size-dependent bioturbation here, as this would require a complex simulation of marine particle coagulation and disaggregation which is beyond the scope of this paper. Also in cases of oxygen deficiency, we do not stop bioturbation in this model. We address the effect of a change in bioturbation on the sediment ages in a sensitivity experiment further below.

2.5. Advection of Solid Sediment Weight Fractions and Sediment Accumulation

[16] The vertical advection of sediment is simulated on the concept of volume conservation for each discrete sediment layer in the bioturbated zone. During simulation, the combined effects of deposition of clay, $CaCO_3$, opal and POC onto the sediment surface, and dissolution of the solid sediment constituents ($CaCO_3$, opal and POC only) may create either an excess or deficiency of solid volume with respect to the prescribed porosity profile. The model accounts for this in the following way: If, for the entire bioturbated sediment zone, the particle rain exceeds redissolution (through pore water reactions and diffusive of pore water transport back into the bottom water column overlying the sediment), this results in a solid fraction volume (i.e., volume of clay, $CaCO_3$, opal and POC) that exceeds the volume prescribed by the porosity profile. In this case the layer's solid constituents will be shifted to the layer below, each in proportion to the excess of volume occupied. This process is repeated successively; the last bioturbated layer's excess volume is finally buried in the consolidated layer. In cases where dissolution of sediment exceeds particle rain from above, sediment starts to erode, creating a deficiency of solid volume with respect to the prescribed porosity profile. After every time step, the gaps in each sediment layer are analyzed, and biogenic material is allowed to travel upward through the sediment mixed layer. In contrast to *Maier-Reimer et al.* [2005], the algorithm for upward advection used in this study starts at the topmost layer within the sediment bioturbated zone, and successively fills the gaps in solid material volume (according to the prescribed porosity profile) from the next lower layer. Thus only material from the next following lower layer is allowed to be transported upward; by doing so, we decrease the artificial upward diffusion of solid constituents that occurs if the algorithm would start from the lowermost reactive layer in the bioturbated sediment. Should the last (deepest) layer within the bioturbated zone still show gaps in its solid material volume, inert (clay) material is eroded from below the sediment mixed layer. The sediment advection for different cases of (1) burial greater than rain minus redissolution (accumulation of sediment) and (2) burial less than rain minus erosion of sediment is illustrated in Figure 2. The vertical velocity w of sediment advection (see equation (11)) is thus a prognostic variable dependent on the sediment deposition

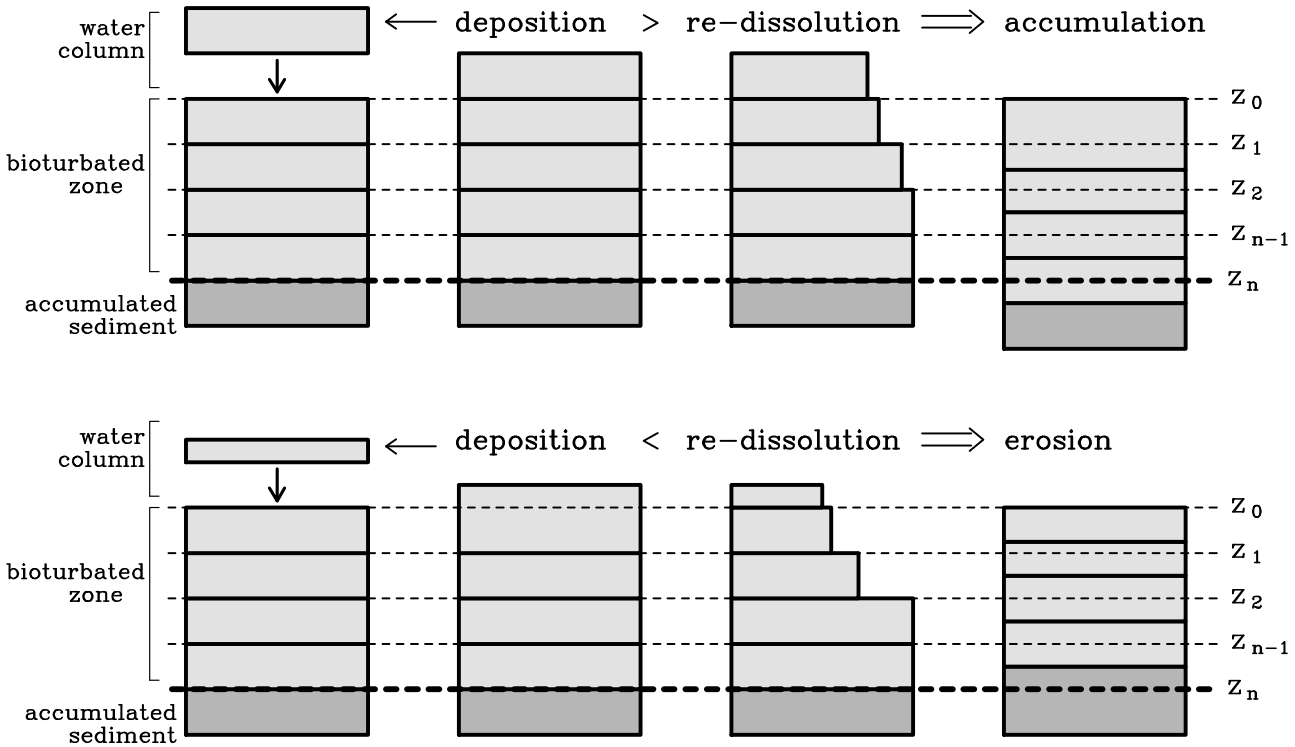

Figure 2. Simulation scheme for sediment advection for different cases of (top) burial greater than rain minus redissolution (accumulation of sediment) and (bottom) burial less than rain minus erosion of sediment. The boundaries of the different model layers in the bioturbated zone are marked by $z_0 \ldots z_n$. Dark grey shading indicates solidified material below the bioturbated zone. Lighter grey shading indicates bioturbated material. The geometric depth level z_n dividing the bioturbated zone from the solidified sediment is represented by the thick dashed line.

from the water column and the pore water chemical reactions.

2.6. Transport of Age Information and Passive Tracers in the Sediment

[17] The age of each sedimentary weight fraction is simulated directly following the sediment accumulation, pore water chemistry, and bioturbation schemes. The particulate material settling onto the top sediment from the water column is associated with the actual model year (calendar year corresponding to the time step, vintage year). This age tracer is then transported with the respective weight fraction as a passive tracer and follows all quantitative modifications of the solid material. For each three-dimensional solid sedimentary material species, thus a three-dimensional age tracer array is introduced. Ultimately, the model is initialized with clay only sediment of age 0. Throughout the integration of the model, it builds up its dedicated biogenic sediment and clay sediment according to dust deposition. In parallel the age structure of each solid weight fraction is established. In order to ensure, that the model is in quasi-equilibrium, we integrated it for 200,000 years.

[18] The ocean model considers only open ocean domains. The annually averaged particle fluxes cannot lead to varved sediments with a seasonal resolution as they occur in restricted areas of the world ocean in reality (such as high-productivity upwelling regimes). Also we use a relative simple representation of the organic carbon cycle and neither consider anoxic process nor the marine nitrogen cycle (including nitrification and denitrification). These extensions, however, can be added to the modeling approach without any complication if needed and if the computational resources are increased. Further, we do not consider here sediment focusing, horizontal sediment transport, and physical mixing of solid sediment compounds or pore waters induced by turbulent motion in the water column.

3. Results for Steady State

[19] The model was integrated over 200,000 years forward in time restarting from clay-only sediment in the bioturbated zone. The initial age of solid material in the top sediment was set to 0 in all ten layers within the bioturbated zone. The resulting solid sediment fractions (Figure 3) as averaged over the top 10 cm of the sediment show about the same results as in earlier studies [*Heinze et al.*, 1999, 2003] with smaller differences due to the revised sediment accumulation scheme, the revised $CaCO_3$ water column dissolution method, and the use of the dust deposition field from *Mahowald et al.* [1999] for the clay flux through the water column. The $CaCO_3$ sediment distribution follows the depth level of the simulated $CaCO_3$ lysocline which is mainly determined through by the

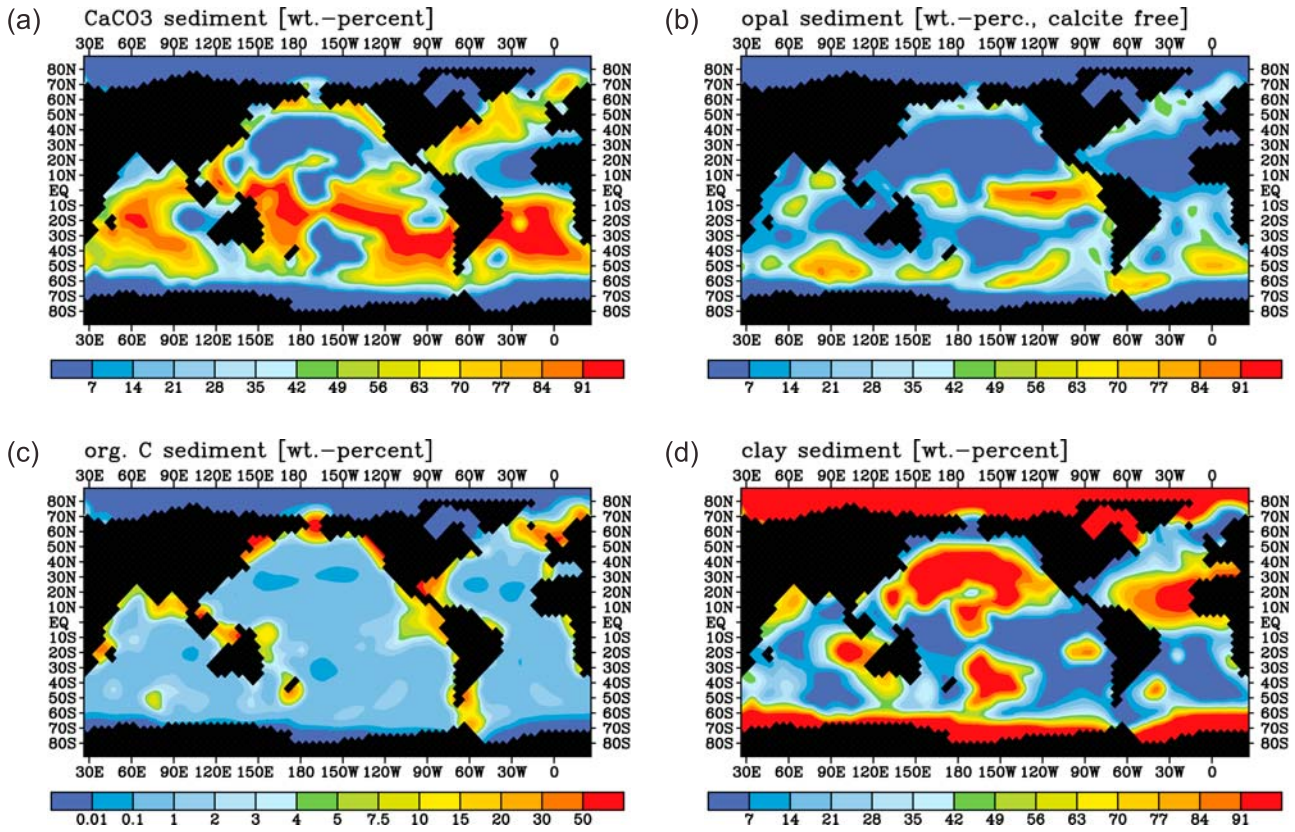

Figure 3. Modeled sediment weight percentages as averaged over the entire bioturbated zone: (a) $CaCO_3$, (b) opal (biogenic silica, with respect to calcite free basis), (c) organic carbon, and (d) clay.

CO_3^{2-} concentration, the latter being rendered quite satisfactorily by the model (Figure 4). The opal sediment shows maxima in upwelling areas such as the equatorial Pacific Ocean and the Southern Ocean. The organic carbon sediment distribution shows only minor weight fraction contributions in open ocean waters and higher concentrations mainly in shallow sea areas. The clay sediment finally reflects the dust field (with a possibly overestimated

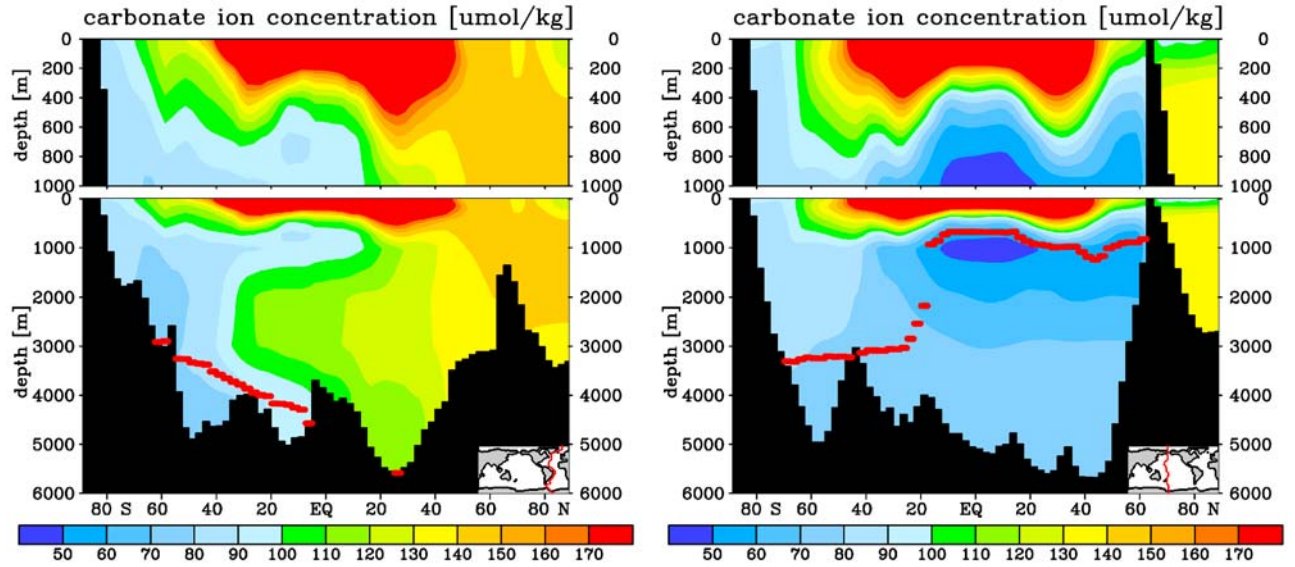

Figure 4. Meridional carbonate ion cross sections (μmol kg^{-1}) for the model standard run ((left) Atlantic and (right) Pacific). The thick red line shows the depth level of the critical carbonate ion concentration [*Broecker and Takahashi*, 1978] indicating the lysocline depth level.

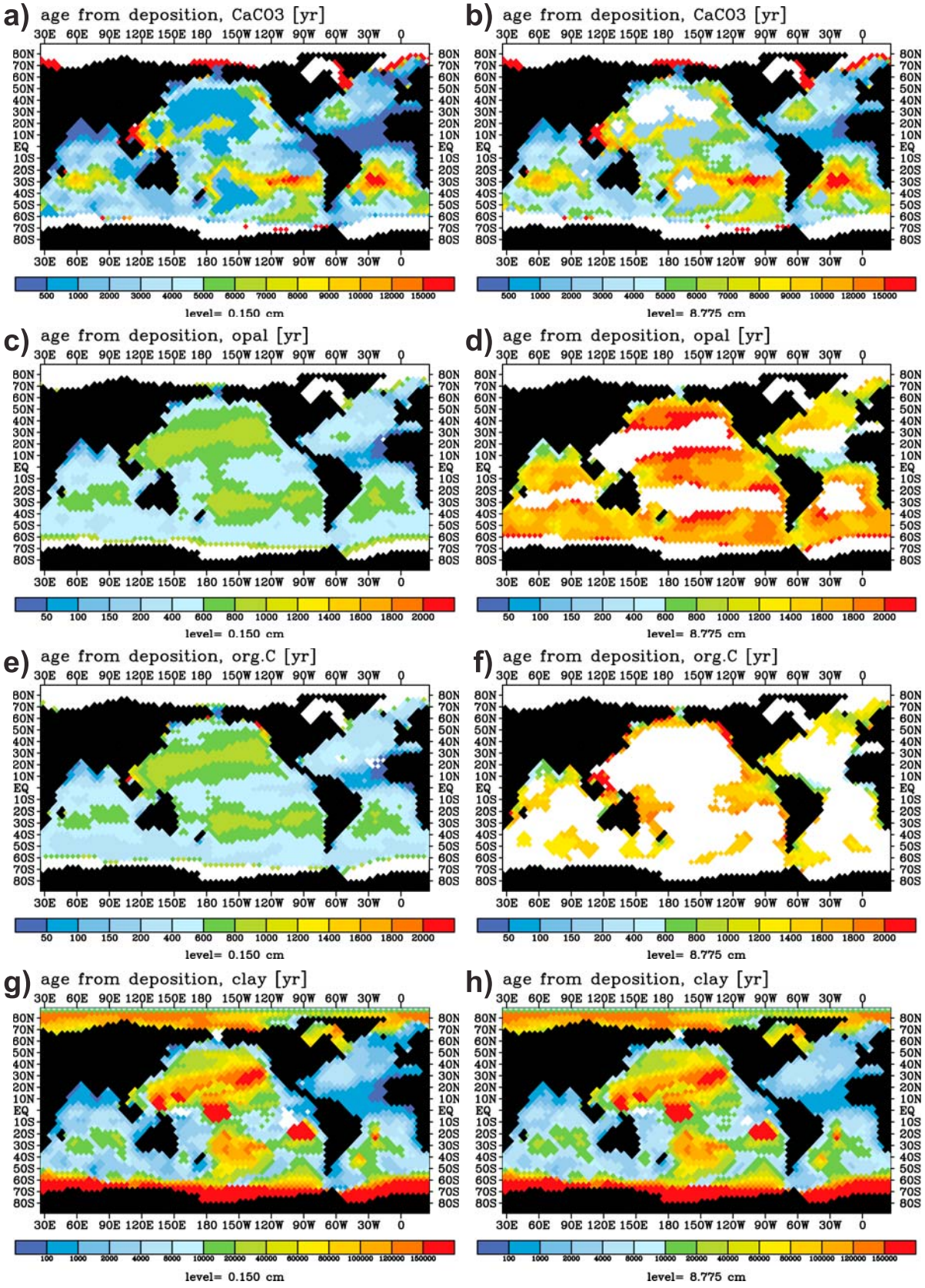

Figure 5. Simulated weight fraction ages in the bioturbated zone where wt % > 0.25% ((left) 0.15 cm and (right) 8.775 cm depth): (a and b) $CaCO_3$, (c and d) opal (on calcite free basis), (e and f) organic carbon, and (g and h) clay (note different color codes for different weight fractions).

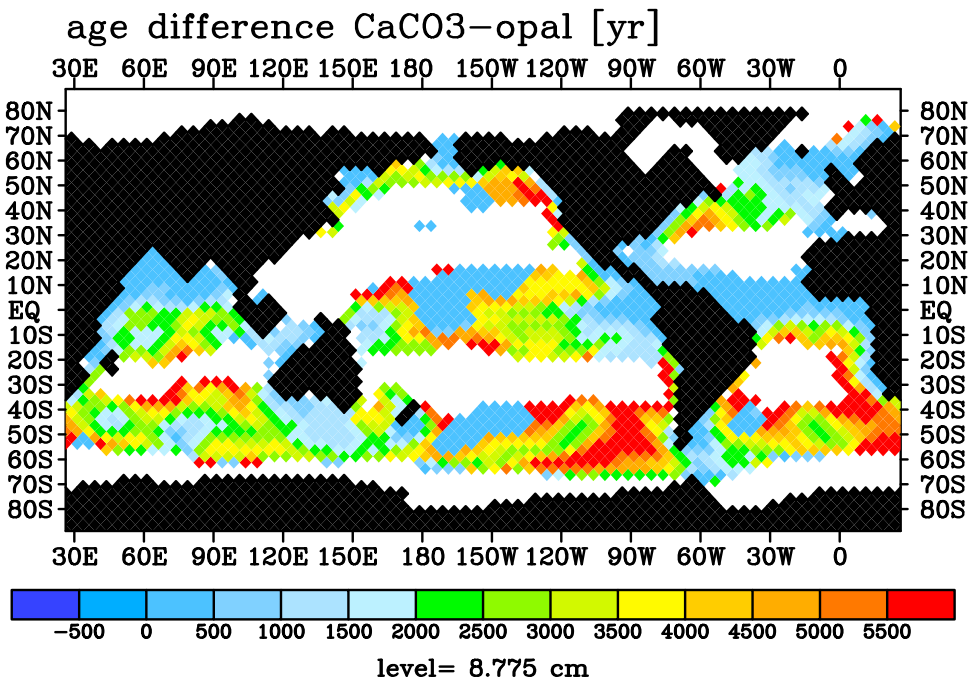

Figure 6. Difference in simulated time intervals from deposition between $CaCO_3$ and opal in the deepest layer of the bioturbated zone. At locations where one or both weight percentages amounted to a value below a threshold of 0.25%, no difference was computed and values were excluded from plotting.

Saharan dust fan in the Atlantic Ocean) and the near absence of biogenic material in areas of the northern Pacific Ocean sediment cover. The sediment distributions compare to first order well with data compilations based on observations for $CaCO_3$ [*Archer*, 1996], opal [*Leinen et al.*, 1986], and organic carbon [*Jahnke*, 1996]. The overestimation of organic sediments in the Gulf of Panama can be attributed by the lack of inorganic pore water chemistry in the present model configuration and the too high export productivity in the area due to nutrient trapping [*Najjar et al.*, 1992; *Aumont et al.*, 1999]. Generally, in this coarse resolution study, gradients in water column as well as in sedimentary tracer distributions are somewhat weaker than in reality due to the smoothed topography.

[20] The simulated ages (time interval from deposition) of the sediment weight fractions show two major features (Figures 5a–5h): (1) each weight fraction shows remarkable horizontal and vertical differences in sediment ages and (2) the ages of different weight fractions at the same location and depth downcore do generally not agree.

[21] These issues can be explained by different biogenic particle production rates, export rates, dissolution and degradation processes in both water column and sediment, as well as gradients in the atmospheric dust deposition. Areas with high accumulation rates in the sediment in general show younger sediment ages than areas with only minor accumulation rates. As the clay sediment is treated here as inert and is only used for "dilution of biogenic sediment" it almost reveals no vertical age structure. It is mainly "old" sediment except for regions with very high dust deposition. $CaCO_3$ shows a more pronounced vertical aging gradient, especially in regions with high saturation and accumulation in the North Atlantic. Organic carbon and opal show relatively strong vertical gradients which are coupled to the reaction rates. The few uppermost centimeters in the bioturbated zone are areas of intense chemical redissolution and degradation processes in areas where the vertical pore water profiles also show strong gradients and have not yet reached asymptotic equilibrium values.

[22] The differences in the age of the various weight fraction species at one location and depth level can be quite significant as is shown in Figure 6 for the age difference between $CaCO_3$ and opal at the lowermost depth level within the model's bioturbated zone (just over the boundary to the nonreactive accumulated "solidified" sediment following further down). The differences can amount to up to several thousands of years. This fact can have considerable consequences for the dating of marine sediment core data, as it is usual practice to associate one geometric depth level in the sediment cores with one unique age for all weight fractions (see also section 5). Potentially, the "true" age of the opal fraction, however, can deviate considerably from the age that has been, e.g., inferred from radiocarbon dating of the calcareous fraction. In order to identify the major reason for the age offset between $CaCO_3$ and opal, we analyzed the relation between the local total mass accumulation and the age offset. Already comparing the age offset (Figure 6) with a map of the total mass accumulation rates (Figure 7) indicates, that the offset is small in high accumulation rates and large in areas of low accumulation. This is corroborated by the quasi-exponential increase in $CaCO_3$-opal age offsets when this offset is plotted directly against the accumulation rates (Figure 8). On the average, a larger proportion of the opal deposited to the sediment

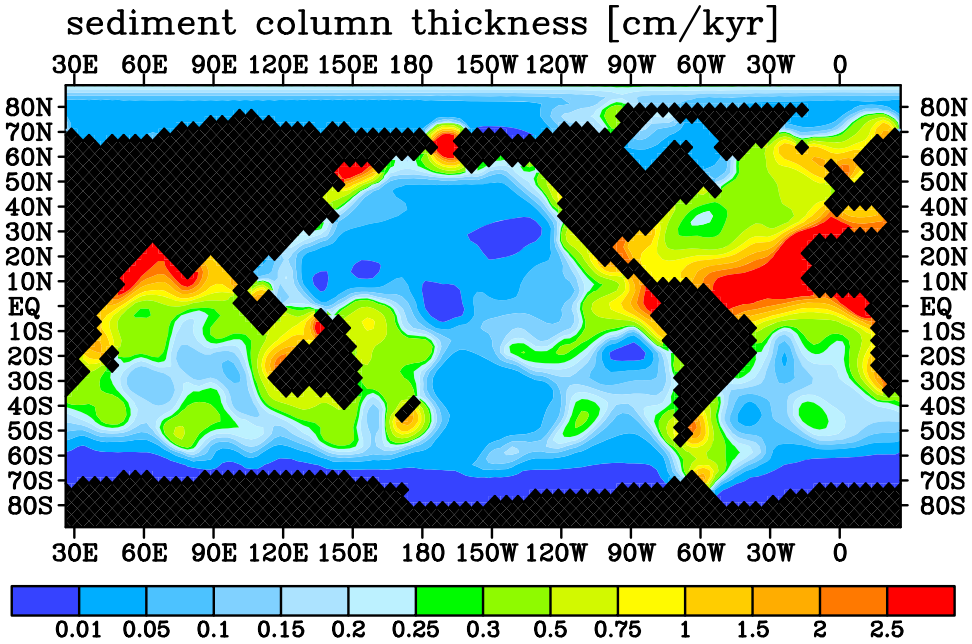

Figure 7. Mass accumulation rates given in terms of the sediment column thickness accumulating per 100,000 years for the control run.

surface is later on redissolved through pore water interaction within the bioturbated zone as compared to $CaCO_3$ (see also the global bulk numbers on deposition, redissolution, and accumulation in Table 2). The lower the accumulation rates (and deposition rates) are, the more efficient the quicker redissolution of opal as compared to $CaCO_3$ is, thus increasing the age offset.

[23] The vertical age structure for the standard run is synthesized in Figure 9, where it can be deduced on how often a certain age occurs for each weight fraction species and each layer in the model's bioturbated zone. Figure 9 shows the "age spectrum" with depth, where the sharpest definition of the ageing within the bioturbated zone results for the highly reactive organic material and opal, while the less reactive $CaCO_3$ ($CaCO_3$ dissolution would mainly occur where the pH within the pore waters is lowered by organic matter remineralization) and inert clay show a broader age spectrum. This more smoothed distribution is a consequence of the differential rain rates and the different accumulation rates, while the reaction rates of the material play a minor ($CaCO_3$) or no (clay) role.

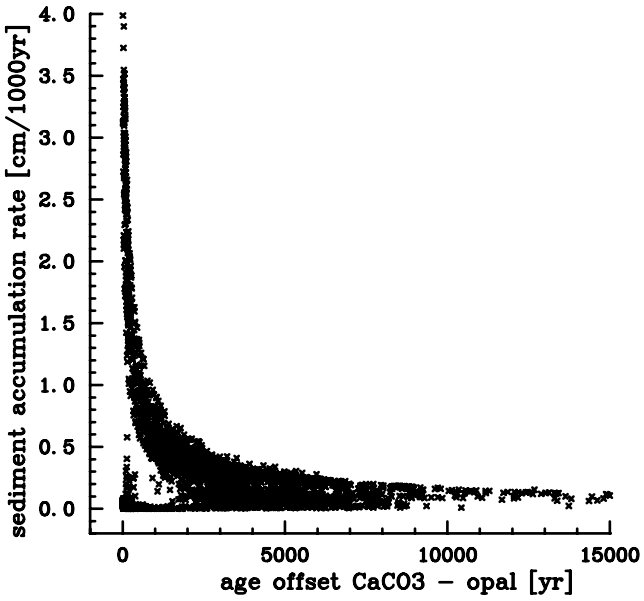

Figure 8. $CaCO_3$-opal age offset versus sediment accumulation rate.

4. Results of Sensitivity Experiments

[24] We carried out a series of sensitivity experiments in order to learn more about the reasons for the age offsets. All

Table 2. Global Gross Values as Resulting for the Model Control Run and the Run With Second-Order Dissolution Kinetics for $CaCO_3$[a]

Global Value	Control Run Value	Second-Order Kinetics
Atmospheric pCO_2 (μatm)	279.1	279.1
POC export production (GtC yr^{-1})	8.52	8.51
POC deposition to sediment (GtC yr^{-1})	0.208	0.208
POC accumulation in sediment (GtC yr^{-1})	0.059	0.060
$CaCO_3$ export production (GtC yr^{-1})	1.23	1.13
$CaCO_3$ deposition (GtC yr^{-1})	0.239	0.274
$CaCO_3$ accumulation (GtC yr^{-1})	0.179	0.210
Opal export production (tmol Si yr^{-1})	189	190
Opal deposition (tmol Si yr^{-1})	68.2	68.4
Opal accumulation (tmol Si yr^{-1})	4.50	4.50

[a]Each run is after 200,000 years of integration.

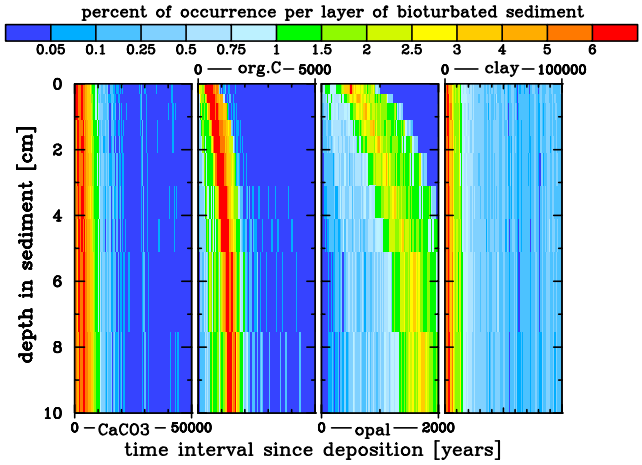

Figure 9. Time intervals from deposition for the four weight fractions (from left to right for $CaCO_3$, organic carbon, opal, and clay) versus depth in the sediment bioturbated zone for the standard run of the model. Please note that the age scale varies for the different weight fractions. The color fill indicates the spread and frequency of certain sediment component ages. Each colored area indicates what percent of all occurrences of valid sediment ages per sediment layer is found in the respective age and depth interval.

experiments (with exception of the time-dependent experiment) were carried out in the same way as the control run and integrated over 200,000 years.

4.1. Experiments on Bioturbation and Opal Dissolution Rate

[25] We will now first test, what influence different reaction rate constants and the strength of bioturbation have on the age distribution of the solid weight fractions in the bioturbated zone. We carried out two quite drastic sensitivity experiments on bioturbation, where we first switched almost off explicit bioturbation by decreasing the bioturbation coefficient to 1% and secondly increased the bioturbation coefficient by a factor of 100 (this coefficient represents the vertical diffusion coefficient for solid matter). In the first case, only vertical sediment advection and numerical diffusion due to the discrete vertical spatial steps shift material downward in the sediment. The second case turns the bioturbated zone into an almost perfectly vertically mixed zone. Further we changed in two experiments the dissolution rate constant for dissolution of opal within the bioturbated zone, we first reduced the rate constant by 50% and then increased it by 50%. For each experiment, the model was integrated from the same initial conditions as in the standard run. The results are summarized in Figures 10a–10d.

[26] The effect of a strong reduction in bioturbation is a higher frequency of old sediments for all four sediment weight fractions when compared with the standard run (see Figures 10a and 9) deeper down in the first 10 cm of sediment. In the few uppermost layers, however, an apparent tapering of the sediment ages occurs. No older material is transported any more upward through bioturbation and only in case of high particle rain rates of reactive material, the latter can survive at the very top of the sediment. The ageing process due to lack of bioturbation increases then further downcore. The shift to the tail on the side of very large sediment ages can clearly be seen for $CaCO_3$ and clay. For strong acceleration of bioturbation, the vertical age structure practically vanishes (Figure 10b). The more reactive sediment weight fractions such as opal get buried more quickly as in the standard run.

[27] The increase and decrease of the sedimentary opal redissolution rate constant have a comparatively minor implication for the ageing process within the bioturbated zone. A smaller rate constant leads to a somewhat older opal sediment with a less well focused age profile (Figures 10c and 10d). The decrease in the rate constant shifts the redissolution of opaline material downcore toward older material. In concert with the bioturbation an on the average larger opal sediment age results. Interestingly, also the age of the $CaCO_3$ sediment weight fraction changes (and to some degree also the organic carbon and clay fractions), if the opal redissolution rate constant is varied. Faster redissolution kinetics for opal result in a shift toward higher ages downcore for the other weight fractions. For opal, the shift toward younger ages in this case is explained by the fact that only somewhat younger opaline material in high-deposition areas has now a chance to survive redissolution. Overall, in the latter case, the total sediment accumulation slows down. Further, in the model, the biogenic export production of $CaCO_3$ is tied to the availability of silicic acid in the ocean surface layer. When not enough silicic acid is available to fuel diatom growth, biogenic production of $CaCO_3$ starts in parallel to silicic acid depletion. A higher redissolution rate of opal from the ocean bottom, thus holds more silicic acid in the water column. This leads to a shift toward higher opal export production rates and lower $CaCO_3$ export production rates from the ocean surface layer. This also can explain the larger age of the $CaCO_3$ weight fraction for an increase in sedimentary opal dissolution.

4.2. Experiment on $CaCO_3$ Dissolution Kinetics

[28] In order to test the effect of different dissolution kinetics for $CaCO_3$, we further carry out an experiment where we replaced the first-order dissolution scheme by a second-order scheme. While first-order dissolution kinetics have been proposed by *Hales and Emerson* [1997], a more recent study suggests a high-order scheme with second-order kinetics being about in the middle of the possible range [*Gehlen et al.*, 2005]. In order to achieve the same atmospheric CO_2 concentration as in the control run, we had to slightly adjust the rain ratio parameter for the $CaCO_3$ export and the carbonate throughput rate (see Table 2). The switch of dissolution kinetics has only a minor impact on the age distribution for $CaCO_3$ sediment, leading to slightly younger sediment ages and a compaction of the age spectrum (less "very old" $CaCO_3$ weight fractions) (Figure 11).

4.3. Time-Dependent Experiment on Signal Rendering

[29] Finally, we carry out a time-dependent experiment in order to test what implications the blurring of the age

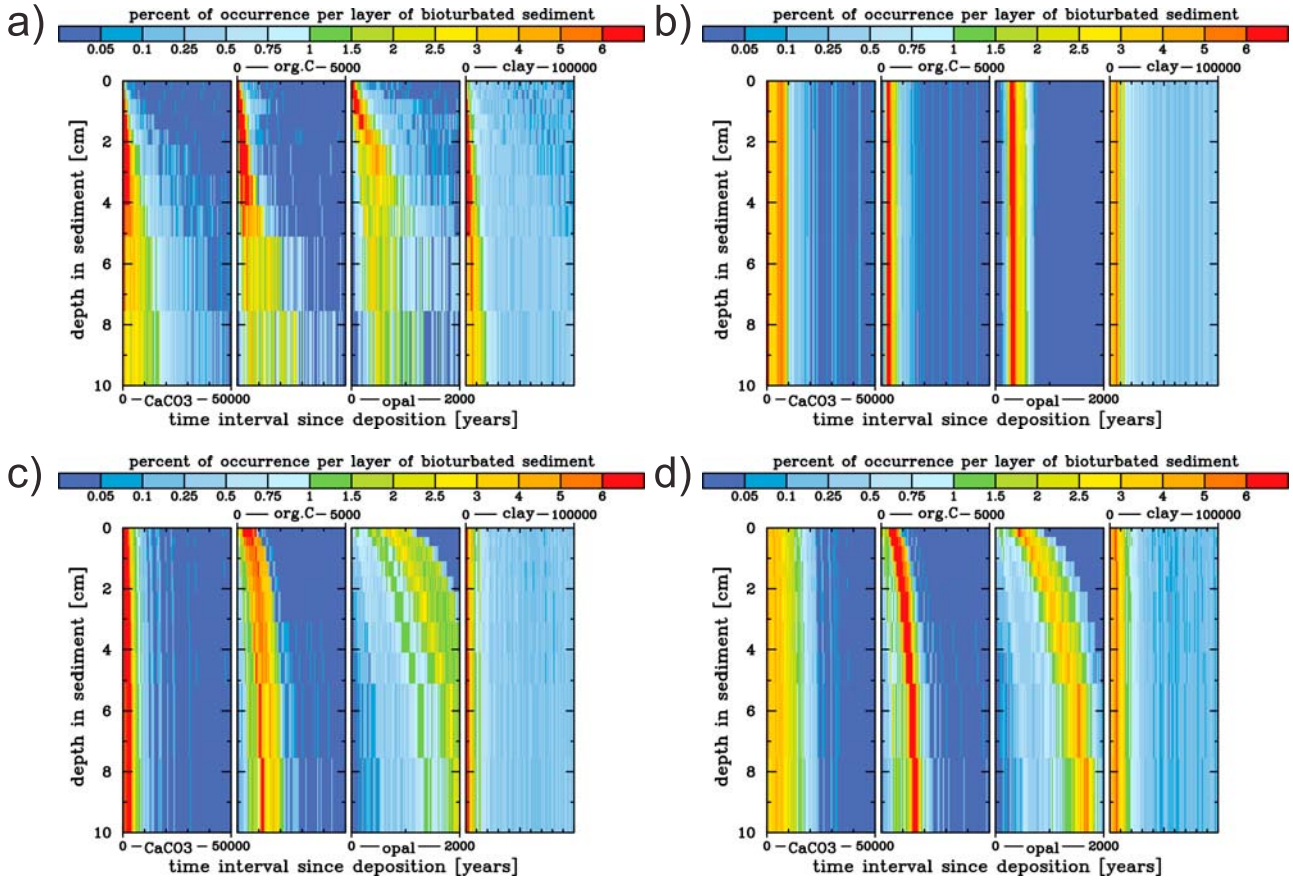

Figure 10. Time intervals from deposition for the four weight fractions as in Figure 6, but for different sensitivity experiments, where the following changes have been made with respect to the standard run: (a) no bioturbation (only numerical diffusion and accumulation), (b) bioturbation 100 times faster, (c) redissolution rate constant for opal in the sediment reduced by 50%, and (d) redissolution rate constant for opal in the sediment increased by 50%.

information within the bioturbated sediment zone has on reproducing climatic signals. It is beyond the scope of this paper to provide a realistic reconstruction of real time-dependent climatic change in the ocean. We rather pursue a simple and "drastic" experiment, that should reveal some of the implications of the $CaCO_3$-opal age offset for the interpretation of sediment core data and their combination with models. In our experiment, we restart from the control run state at year 200,000 and continue the integration for further 50,000 years. During years 20,000–30,000 we halved the velocity components of the three-dimensional flow field and also halved the convective adjustment mixing. This somewhat artificial experiment leads to a clear signal in biogenic surface production rates and a respective clear signal in the sediment. The 20,000 years with normal flow field conditions before and after the slowing down serve as buffers to watch the respective behavior of the sediment accumulating. During the slowing down of the ocean circulation all globally averaged biological production rates as well as the atmospheric CO_2 concentration where reduced as expected for a more efficient biological pump under a more sluggish oceanic flow field. We pick three different sites for analyzing the age offset and the way the "climatic" perturbation signal is transferred to the sediment record: (1) the eastern equatorial Pacific Ocean (1.25°S, 91.25°W), (2) the midlatitudes of the Indian Ocean (46.25°S, 93.75°E), and (3) the western North Atlantic (36.25°S, 68.75°W). The first region shows fairly high sediment accumulation rates, the two other sites are marked by relative slow sediment accumulation. While in the low-accumulation sites the biogenic export production for $CaCO_3$ and opal both decrease during the slow down of the circulation, the $CaCO_3$ export increases for the equatorial Pacific due to our parameterization of the $CaCO_3$ export production (onset after depletion of silicic acid) (see fourth plots from left in Figures 12a–12c). At the three sites, sediment cores were recovered from the model data set accumulating under the bioturbated zone over the 50,000 years of integration. The age offset between $CaCO_3$ and opal is close to zero for the higher-accumulation upwelling region and increases drastically for the Indian and Atlantic low-accumulation examples, where the $CaCO_3$ signal leads the opal signal by about 5000 years. In general, the surface signal is smeared out in the sediment cores and leads to an early bias which increases with sediment age. This means, that due to bioturbation, sedimented material is always

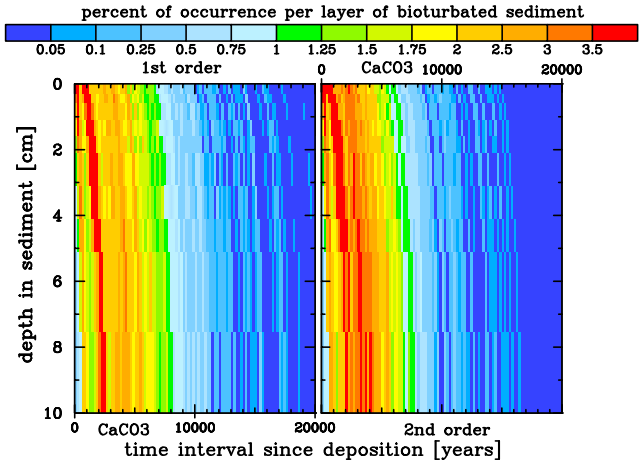

Figure 11. Time intervals from deposition for the four weight fractions as in Figure 6 but for $CaCO_3$ only and only for time interval 0–20,000 years. (left) The frequency of the $CaCO_3$ age occurrences for the standard run using first-order redissolution kinetics. (right) Diagram from a model run using second-order redissolution kinetics (adjusted to the same atmospheric pCO_2 as in the standard run which was achieved through slight corrections of the rain ratio parameters and the continental carbonate flux).

mixed with older material which has been deposited earlier. Taking especially the $CaCO_3$ ages as benchmark for correcting the opal ages would also render the situation for the opal ages worse, as the opal age bias would be increased to the $CaCO_3$ bias (compare the second and third plots from left in Figures 12a–12c). The analysis, however, indicates that the $CaCO_3$-opal age offset seems to be ameliorated or even unproblematic in high-accumulation regions where the differential reactivities of different weight fractions are overridden by a quick enough sediment deposition and accumulation rate (i.e., the bioturbated zone is so quickly "flushed," that differences in the reaction rates do not matter so much for the age distribution). In low-accumulation regions, especially those with dominating $CaCO_3$ fraction and only small amounts of opal, the age differences between both fractions can be misleading.

5. Discussion

[30] Differential ages of different sediment weight fractions obviously can result due to the rain rates of the various materials to the ocean floor, the reactivity of the material, the dissolution kinetics, and the bioturbation strength. Critical to age offsets between different weight fractions is the mass accumulation rate: The smaller the accumulation rate is, the more efficient are differences in redissolution rates among different weight fractions in order to increase the age offset. There is few evidence from observations around, which can be used for comparison. The reason for this is the difficulty to directly determine the age of opaline or clay sediment. Recent studies [e.g., *Ingalls et al.*, 2004; *Hatté et al.*, 2008], however, may open up new possibilities to determine the age of diatomaceous sediments through ^{14}C dating of proteins which are enclosed by the diatom shell material. As both, $CaCO_3$ and organic carbon include all three carbon isotopes(^{12}C, ^{13}C, and ^{14}C) as part of the weight fraction the situation is here somewhat better. From $\Delta^{14}C$ measurements of calcareous shell material and the organic carbon weight fraction observed in sediment cores, approximate ages of these materials can be directly inferred even from very small samples [*Pearson et al.*, 1998].

[31] Differential ages of sedimentary material have been reported and attributed to resuspension of fine grained material [*Haidar et al.*, 2000] and lateral transport [*Mollenhauer et al.*, 2007] of resuspended organic material. In our modeling study, neither differential particle size fractions, nor sedimentary transport including resuspension are considered. The study of *Mollenhauer et al.* [2007] reports in most cases younger conventional radiocarbon ages for the organic material than for the calcareous fraction in sediment samples from the Benguela upwelling system. These samples from the upper centimeters of the sediment cores compare favorably with the general trends found here (Figures 6 and 9), both for the order of magnitude of the organic carbon age and the CO_3 age, as well as their age difference (with the organic carbon ages being younger than the calcareous material ages in most cases). This indicates, that also weight fraction specific differences in pore water reactions as well as differential rain rates can cause differential weight fraction ages in the sediment. *Ingalls et al.* [2004] report the possibility of differential ages of diatomaceous and foraminiferal material for Southern Ocean sediments in both directions (either positive or negative differences). This behavior is in general agreement with our findings here, that considerable age differences can occur for $CaCO_3$ and opal sediment at the time of sediment accumulation (at the lower boundary of the bioturbated zone). Figure 6 shows similar orders of magnitude for these differences as reported by *Ingalls et al.* [2004] and indicates that horizontally steep gradients of these age differences can occur, though we do not find younger $CaCO_3$ than opal phases, which can be due to specific locally important processes such as resuspension and bottom water flows not included in our model. Therefore, our model study clearly confirms their statement: "Therefore, care should be used when interpreting diatom-based paleoproxies in sediment cores that have chronologies based on foraminif-

Figure 12. Analysis of three sites for the signal transmission of export production signals during a slowing down of ocean circulation between years 30,000 and 20,000 before the end of model integration: (a) eastern equatorial Pacific Ocean (1.25°S, 91.25°W), (b) midlatitudes of the Indian Ocean (46.25°S, 93.75°E), and (c) western North Atlantic (36.25°S, 68.75°W). From left to right: Downcore distribution of wt % of $CaCO_3$ and opal, same values plotted against their own specific weight fraction age, both $CaCO_3$ and opal plotted against the age of the $CaCO_3$ fraction, and export production rates. Please note the differing *x* axis and *y* axis scales.

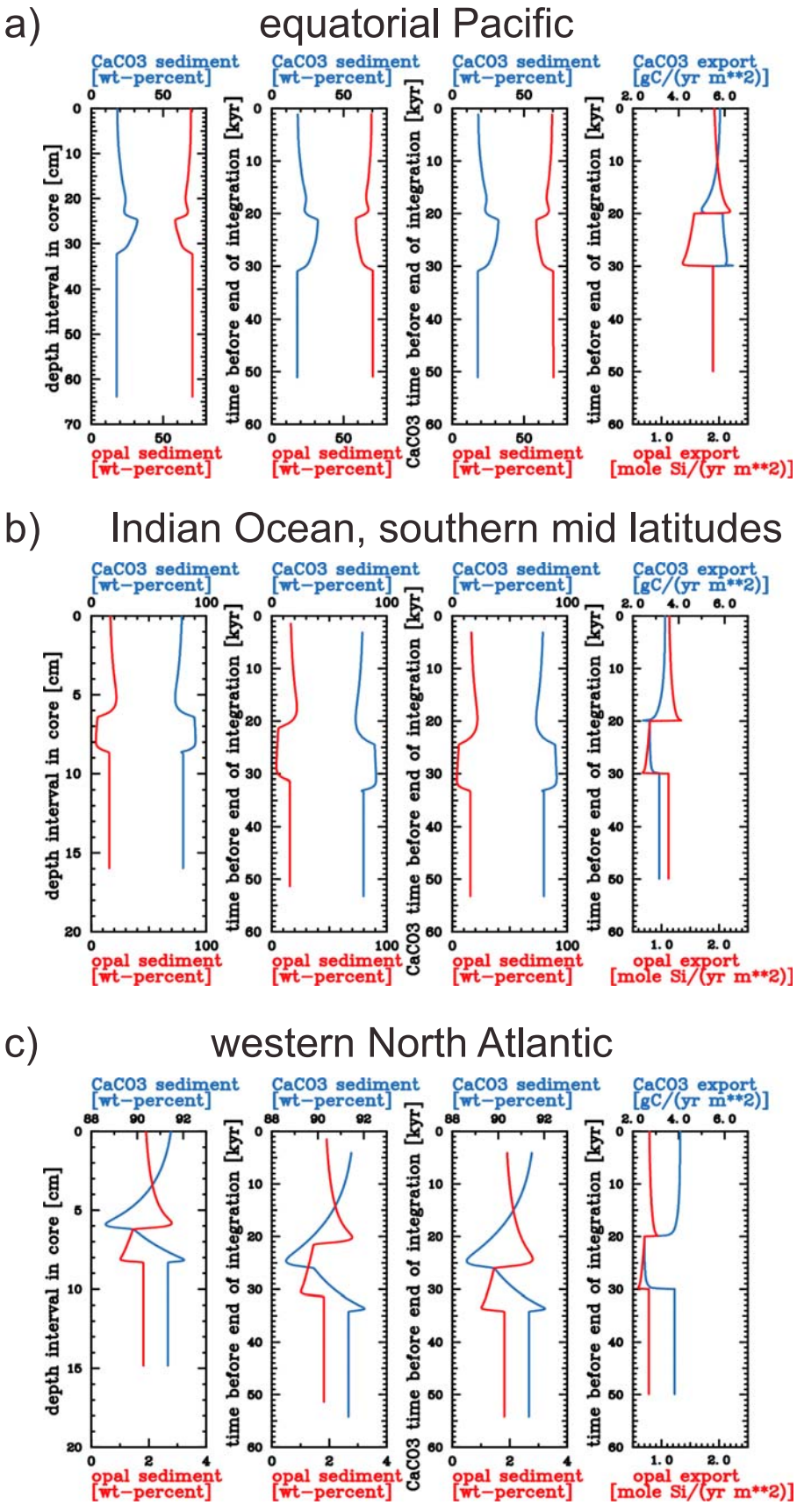
a) equatorial Pacific
b) Indian Ocean, southern mid latitudes
c) western North Atlantic
CaCO3 sediment [wt-percent]
CaCO3 export [gC/(yr m**2)]
depth interval in core [cm]
time before end of integration [kyr]
CaCO3 time before end of integration [kyr]
opal sediment [wt-percent]
opal export [mole Si/(yr m**2)]

Figure 12

eral ages, as the two mineral phases may not sediment on the same timescale'' [*Ingalls et al.*, 2004, p. 101].

[32] Ultimately, it would be a necessary prerequisite for systematic calibration of Earth system models through the sedimentary paleoclimatic record to correctly simulate the ages of the different sedimentary tracer species as well as determine the correct ages of different weight fractions in sediment samples from real cores. The lack of a suitable age modeling component was listed in the work by *Heinze* [2001] as a gap to be closed before simulated sediment cores can be used on a global basis for data assimilation of the marine paleoclimatic record into climate models. The study here approached a closing of this gap through testing a corresponding methodology. In advanced data assimilation procedures such as the adjoint method, [e.g., *Errico*, 1997; *Giering and Kaminski*, 1998], where one tries to systematically minimize the difference between modeled values and corresponding observations, one can even vary corrections to the original choice of reaction rate constants, bioturbation coefficients, and other governing parameters so that a part of the still existing uncertainties about the age and early diagenesis modeling can be determined trough the data assimilation procedure itself. When these governing parameters are corrected, one should apply this correction everywhere or as part of a process based functional relationship (but not arbitrarily vary the corrections from location to location).

6. Summary and Conclusions

[33] We have here for the first time analyzed the vertical age structure for four different weight fractions of newly formed open ocean sediment simultaneously with a global biogeochemical ocean general circulation model. It turns out that at a given geometric depth level within the bioturbated top sediment zone the ages of different weight fractions generally do not coincide. This confirms the respectively available evidence from real world marine sediment cores. Governing parameters for the distributions of solid sediment compounds and the pore water reactions can change the age distribution of sediment weight fractions downcore. The critical age offset between $CaCO_3$ and opal increases with sinking sediment accumulation rates. This fact may ameliorate the age offset problem for analysis of high-accumulation sediment cores. The methodology of age transport with the various sediment weight fractions can be exploited also as a passive tracer transport algorithm to transport paleoclimatic tracers downcore which are associated with different materials such as $\delta^{13}C$ of organic material, $\delta^{13}C$ or $\delta^{18}O$ of planktonic and benthic foraminifera, as well as radionuclides such as ^{231}Pa and ^{230}Th. Forthcoming attempts to carry out a systematic data assimilation of marine sediment core data into climate models in order to optimally determine their adjustable parameters require solid observational databases. For the measuring paleoclimatic research community, the establishment of such databases which must include the correct synchronization of different sedimentary weight fractions and tracers provides a challenge.

[34] **Acknowledgments.** A part of this work was carried out during a sabbatical at the chemical oceanography group at IFM-GEOMAR in Kiel. The author is grateful to Douglas Wallace and Arne Körtzinger for hosting him during this time. Thanks are due to Arne Winguth (University of Texas at Arlington) for the velocity field of the large-scale geostrophic model. The advice from Pieter Grootes (University of Kiel), Jorijntje Henderiks (University of Stockholm), and Jelle Bijma (Alfred Wegener Institute for Polar and Marine Research) concerning real sediment cores is highly appreciated. Two reviewers kindly helped to improve the original manuscript. This work was partially supported through the University of Bergen (sabbatical funds) through the ''European Project on Ocean Acidification'' which received funding from the European Community's Seventh Framework Programme (FP7/2007-2013) under grant agreement 211384 and through EU FP6 Integrated Project CARBOOCEAN funded by the European Commission under contract 511176 (GOCE). A part of the computations where carried out under project nn2980k at the Norwegian Metacenter for Computational Science NOTUR. This is publication A 249 from the Bjerknes Centre for Climate Research.

References

Archer, D. (1996), An atlas of the distribution of calcium carbonate in sediments of the deep sea, *Global Biogeochem. Cycles*, *10*, 159–174.

Archer, D., M. Lyle, K. Rodgers, and P. Froelich (1993), What controls opal preservation in tropical deep-sea sediments?, *Paleoceanography*, *8*, 7–21.

Aumont, O., J. C. Orr, P. Monfray, G. Madec, and E. Maier-Reimer (1999), Nutrient trapping in the equatorial Pacific: The ocean circulation solution, *Global Biogeochem. Cycles*, *13*, 351–369.

Bard, E. (2001), Paleoceanographic implications of the difference in deep-sea sediment mixing between large and fine particles, *Paleoceanography*, *16*, 235–239.

Boudreau, B. P. (1997), *Diagenetic Models and Their Implementation*, 414 pp., Springer, New York.

Boudreau, B. P., and D. M. Imboden (1987), Mathematics of tracer mixing in sediments: III. The theory of nonlocal mixing within sediments, *Am. J. Sci.*, *287*, 693–719.

Broecker, W. S., and T. Takahashi (1978), The relation between lysocline depth and in situ carbonate ion concentration, *Deep Sea Res.*, *25*, 65–95.

Crowley, T. J. (1990), Are there any satisfactory geologic analogs for a future greenhouse warming?, *J. Clim.*, *3*(11), 1282–1292.

Dixit, S., P. Van Cappellen, and A. J. van Bennekom (2001), Processes controlling solubility of biogenic silica and pore water build-up of silicic acid in marine sediments, *Mar. Chem.*, *73*, 333–352.

Edmond, J. M., and J. M. T. M. Gieskes (1970), On the calculation of the degree of saturation of sea water with respect to calcium carbonate under in situ conditions, *Geochim. Cosmochim. Acta*, *34*, 1261–1291.

Errico, R. M. (1997), What is an adjoint model?, *Bull. Am. Meteorol. Soc.*, *78*(11), 2577–2591.

Gehlen, M., F. C. Bassinot, L. Chou, and D. McCorkle (2005), Reassessing the dissolution of marine carbonates: II. Reaction kinetics, *Deep Sea Res., Part I*, *52*, 1461–1476.

Giering, R., and T. Kaminski (1998), Recipes for adjoint code construction, *Trans. Math. Software*, *24*(4), 437–474.

Grieger, B., and H.-S. Niebler (2003), Glacial South Atlantic surface temperatures interpolated with a semi-inverse ocean model, *Paleoceanography*, *18*(3), 1056, doi:10.1029/2002PA000773.

Haidar, A. T., H. R. Thierstein, and W. G. Deuser (2000), Calcareous phytoplankton standing stocks, fluxes and accumulation in Holocene sediments off Bermuda (N. Atlantic), *Deep Sea Res., Part II*, *47*, 1907–1938.

Hales, B., and S. Emerson (1997), Evidence in support of first-order dissolution kinetics of calcite in seawater, *Earth Planet. Sci. Lett.*, *148*, 317–327.

Hatté, C., G. Hodgins, A. J. T. Jull, B. Bishop, and B. Tesson (2008), Marine chronology based on ^{14}C dating on diatoms proteins, *Mar. Chem.*, *109*, 143–151.

Heinze, C. (2001), Towards the time dependent modeling of sediment core data on a global basis, *Geophys. Res. Lett.*, *28*(22), 4211–4214.

Heinze, C., E. Maier-Reimer, A. M. E. Winguth, and D. Archer (1999), A global oceanic sediment model for long-term climate studies, *Global Biogeochem. Cycles*, *13*, 221–250.

Heinze, C., A. Hupe, E. Maier-Reimer, N. Dittert, and O. Ragueneau (2003), Sensitivity of the marine biospheric Si cycle for biogeochemical parameter variations, *Global Biogeochem. Cycles*, *17*(3), 1086, doi:10.1029/2002GB001943.

Heinze, C., M. Gehlen, and C. Land (2006), On the potential of ^{230}Th, ^{231}Pa, and ^{10}Be for marine rain ratio determinations: A modeling study, *Global Biogeochem. Cycles*, *20*, GB2018, doi:10.1029/2005GB002595.

Ingalls, A. E., R. F. Anderson, and A. Pearson (2004), Radiocarbon dating of diatom-bound organic compounds, *Mar. Chem.*, *92*, 91–105.

Ingle, S. E. (1975), Solubility of calcite in the ocean, *Mar. Chem.*, *3*, 301–319.

Jahnke, R. A. (1996), The global ocean flux of particulate organic carbon: Areal distribution and magnitude, *Global Biogeochem. Cycles*, *10*, 71–88.

LeGrand, P., and C. Wunsch (1995), Constraints from paleotracer data on the North Atlantic circulation during the Last Glacial Maximum, *Paleoceanography*, *10*, 1011–1045.

Leinen, M., D. Cwienk, G. R. Heath, P. E. Biscaye, V. Kolla, J. Thiede, and J. P. Dauphin (1986), Distribution of biogenic silica and quartz in recent deep-sea sediments, *Geology*, *14*, 199–203.

Li, Y.-H., and S. Gregory (1974), Diffusion of ions in sea water and in deep-sea sediments, *Geochim. Cosmochim. Acta*, *38*, 703–714.

Mahowald, N., K. Kohfeld, M. Hansson, Y. Balkanski, S. P. Harrison, I. C. Prentice, M. Schulz, and H. Rodhe (1999), Dust sources and deposition during the Last Glacial Maximum and current climate: A comparison of model results with paleodata from ice cores and marine sediments, *J. Geophys. Res.*, *104*(D13), 15,895–15,916.

Maier-Reimer, E. (1993), Geochemical cycles in an ocean general circulation model: Preindustrial tracer distributions, *Global Biogeochem. Cycles*, *7*, 645–677.

Maier-Reimer, E., I. Kriest, J. Segschneider, and P. Wetzel (2005), The Hamburg Ocean Carbon Cycle Model HAMOCC 5.1: Technical description release 1.1, *Ber. Erdsyst. 14*, 50 pp., Max Planck Inst. for Meteorol., Hamburg, Germany.

Mehrbach, C., C. H. Culberson, J. E. Hawley, and R. M. Pytkowicz (1973), Measurement of the apparent dissociation constants of carbonic acid in seawater at atmospheric pressure, *Limnol. Oceanogr.*, *18*, 897–907.

Mikolajewicz, U., M. Gröger, E. Maier-Reimer, G. Schurgers, M. Vizcaíno, and A. M. E. Winguth (2007), Long-term effects of anthropogenic CO_2 emissions simulated with a complex Earth system model, *Clim. Dyn.*, *28*(6), 599–631.

Mollenhauer, G., M. Inthorn, T. Vogt, M. Zabel, J. S. Sinninghe Damsté, and T. I. Eglington (2007), Aging of marine organic matter during cross-shelf lateral transport in the Benguela upwelling system revealed by compound-specific radiocarbon dating, *Geochem. Geophys. Geosyst.*, *8*, Q09004, doi:10.1029/2007GC001603.

Najjar, R. G., J. L. Sarmiento, and J. R. Toggweiler (1992), Downward transport and fate organic matter in the ocean: Simulations with a general circulation model, *Global Biogeochem. Cycles*, *6*, 45–76.

Parsons, T. R., and M. Takahashi (1973), *Biological Oceanographic Processes*, 186 pp., Pergamon, Oxford, U. K.

Pearson, A., A. P. McNichol, R. J. Schneider, K. F. Von Reden, and Y. Zheng (1998), Microscale AMS ^{14}C measurement at NOSAMS, *Radiocarbon*, *40*(1), 61–75.

Ridgwell, A. (2007a), Interpreting transient carbonate compensation depth changes by marine sediment core modeling, *Paleoceanography*, *22*, PA4102, doi:10.1029/2006PA001372.

Ridgwell, A. (2007b), Application of sediment core modelling to interpreting the glacial-interglacial record of Southern Ocean silica cycling, *Clim. Past*, *3*, 387–396.

Smith, C. R., and C. Rabouille (2002), What controls the mixed-layer depth in deep-sea sediments? The importance of POC flux, *Limnol. Oceanogr.*, *47*, 418–426.

Ullmann, W. J., and R. C. Aller (1982), Diffusion coefficients in nearshore marine environments, *Limnol. Oceanogr.*, *27*, 552–556.

Weiss, R. F. (1970), The solubility of nitrogen, oxygen, and argon in water and seawater, *Deep Sea Res. Oceanogr. Abstr.*, *17*, 721–735.

Weiss, R. F. (1974), Carbon dioxide in water and seawater: The solubility of a non-ideal gas, *Mar. Chem.*, *2*, 203–215.

Winguth, A. M. E., D. Archer, J.-C. Duplessy, E. Maier-Reimer, and U. Mikolajewicz (1999), Sensitivity of paleonutrient tracer distributions and deep sea circulation to glacial boundary conditions, *Paleoceanography*, *14*, 304–323.

C. Heinze, Geophysical Institute, University of Bergen, Allégaten 70, N-5007 Bergen, Norway. (christoph.heinze@gfi.uib.no)

I. Kriest, Leibniz Institute of Marine Sciences at University of Kiel (IFM-GEOMAR), D-24105 Kiel, Germany.

E. Maier-Reimer, Max Planck Institute for Meteorology, D-20146 Hamburg, Germany.